minerals

MDPI

Article

Integrating AlphaEarth Foundation Embeddings and GF-5 Hyperspectral Features for Lithological Classification and Cross-Regional Mapping

Chang Xu [1,2], Peng Zhang [1,3,*], Yongcheng Lin [2,*], Bin Wang [2,4], Lei Chen [5] and Peng Xun [2]

[1] School of Civil Engineering, Qingdao University of Technology, Qingdao 266520, China; xuchang881115@163.com
[2] Shandong Key Laboratory of Deep Earth Resources Exploration and Evaluation, Technology Innovation Center for Deep Gold Deposit Exploration and Mining, Ministry of Natural Resources, No.6 Geological Team of Shandong Provincial Bureau of Geology and Mineral Resources, Weihai 264209, China; wangbinjlu@163.com (B.W.); sddkxp@163.com (P.X.)
[3] Engineering Research Center of Concrete Technology Under Marine Environment, Ministry of Education, Qingdao University of Technology, Qingdao 266520, China
[4] School of Earth Sciences and Resources, China University of Geosciences, Beijing 100083, China
[5] Faculty of Geography, Tianjin Normal University, Tianjin 300387, China; lchen@tjnu.edu.cn
* Correspondence: zhangpchn@qut.edu.cn (P.Z.); maillych@163.com (Y.L.)

Abstract

Accurate lithological mapping is constrained by spectral similarity among rock units, limited field samples, and the weak transferability of classification models across heterogeneous geological environments. Although hyperspectral imagery provides detailed mineralogical information, its high dimensionality and sensitivity to surface conditions limit its ability to represent broader spatial and geological contexts. This study evaluates the potential of AlphaEarth Foundations (AEF) embeddings for lithological classification by integrating 64-dimensional AEF representations with spectral features derived from GF-5 hyperspectral imagery. The hyperspectral feature set comprised diagnostic absorption bands, band-ratio indices, and spectral absorption parameters. Support vector machine (SVMs) and random forest (RF) classifiers were used to assess individual and fused feature configurations, sample-size sensitivity, and cross-regional sample transfer. Among the hyperspectral-only configurations, multi-feature fusion achieved the highest overall accuracies of 75.84% for RF and 71.81% for SVM. AEF embeddings used independently achieved overall accuracies of 76.33% and 78.00% with RF and SVM, respectively, indicating that the pretrained embeddings contain information relevant to lithological discrimination. Feature fusion produced classifier-dependent responses. For RF, combining AEF with band-ratio features yielded the highest accuracy of 79.30% and a Kappa coefficient of 0.656, whereas SVM was more sensitive to the inclusion of individual hyperspectral feature groups. Cross-regional application to adjacent mining areas showed that the transferred classifications broadly preserved the spatial continuity and distribution patterns of major lithological units, although local differences remained for structurally complex units. These results demonstrate that AEF embeddings complement the mineral-sensitive information provided by hyperspectral imagery. Their integration offers a practical strategy for lithological mapping under limited-sample conditions, highlighting the need for classifier-specific feature fusion.

Academic Editor: Bernard Hubbard

Received: 29 October 2026
Revised: 21 November 2026
Accepted: 23 November 2026
Published: 24 November 2026

Copyright: © 2026 by the authors. Licensee MDPI, Basel, Switzerland. This article is an open access article distributed under the terms and conditions of the Creative Commons Attribution (CC BY) license.

Keywords: AlphaEarth Foundations; GF-5 hyperspectral imagery; lithological classification; remote sensing foundation model; feature fusion; cross-regional mapping

1. Introduction

Lithological mapping is fundamental to regional geological investigation, mineral exploration, environmental assessment, and geological hazard analysis. Accurate identification of rock units provides essential information for interpreting geological structures, mineralization processes, and landscape evolution [1]. Conventional geological mapping relies heavily on field surveys, sampling, and drilling, which provide reliable local observations but are costly and difficult to implement consistently over extensive or inaccessible areas [2]. Remote sensing therefore offers an important complementary approach because it enables spatially continuous observations of surface spectral and structural characteristics over large regions. Variations in mineral composition, weathering state, texture, and surface structure produce differences in reflectance, absorption, and scattering responses that can be used to discriminate lithological units [3].

Hyperspectral remote sensing is particularly valuable for lithological analysis because its narrow and contiguous spectral bands can resolve diagnostic absorption features associated with rock-forming and alteration minerals. GF-5 hyperspectral imagery, for example, provides extensive spectral coverage that supports the extraction of representative absorption bands, mineral-related band ratios, and quantitative absorption parameters. By capturing variations in iron-bearing minerals, hydroxyl-bearing minerals, carbonates, and alteration-related mineral assemblages, these spectral features may help distinguish the lithological classes through their combined mineralogical responses.

However, hyperspectral lithological classification remains challenging. Rock units with similar mineral assemblages may exhibit overlapping spectra, whereas weathering, shadows, mixed pixels, vegetation cover, and atmospheric effects can alter their observed responses [4,5]. Moreover, hyperspectral imagery contains substantial redundancy and noise, and manually constructed spectral features may only represent selected aspects of lithological variability [6,7]. These limitations are particularly important when training samples are scarce or when a model is transferred between regions with different surface conditions [8,9].

Machine learning and deep learning methods have improved the extraction and classification of lithological information from remote sensing data. Support vector machines (SVMs) and random forests (RFs) remain widely used because they can handle nonlinear class boundaries and high-dimensional inputs under relatively limited sample conditions [10–12]. Convolutional neural networks (CNNs), transfer-learning approaches, and knowledge-guided architectures further enable the extraction of spatial and semantic information that cannot be fully described by manually designed spectral variables [13]. The integration of hyperspectral imagery and machine learning has also been applied to mineral exploration and alteration mapping, demonstrating the potential of mineral-sensitive spectral information for geological interpretation [14,15].

Nevertheless, the effectiveness of these methods depends strongly on the representativeness of training samples and input features. Models trained in a single geological setting may capture region-specific spectral relationships rather than transferable lithological characteristics, leading to performance degradation when applied to neighboring or environmentally distinct regions.

Multi-source feature fusion provides a potential solution by combining complementary information from different observations or feature domains [2,16,17]. Further research achieved 99.42% classification accuracy for shale lithology using multi-source features and ensemble learning [18]. Ibrahim et al. proposed a novel SMOTE-XGB model, which improved lithological identification, especially for mineralized rock units, compared with conventional classifiers [19]. Li et al. employed transfer learning based on image features to achieve pixel-wise lithological classification of sampled rocks, demonstrating strong robustness and generalization ability. Hyperspectral variables describe fine-scale mineral absorption and alteration characteristics, whereas broader remote sensing representations may encode land-surface context, texture, terrain, climate, and spatial organization [20]. However, simply concatenating heterogeneous features does not necessarily improve classification. Redundant or incompatible variables may increase dimensionality, amplify noise, and affect different classifiers in different ways [21,22]. Consequently, feature fusion should be evaluated not only according to whether classification accuracy increases, but also according to how the contribution of each feature source varies with classifier type, sample size, and regional transfer conditions.

Recent remote sensing foundation models provide a new way for geospatial feature representation. AlphaEarth Foundations generates globally consistent 64-dimensional embeddings by integrating multi-source Earth observation and environmental information through large-scale pretraining. Unlike conventional spectral features designed for a specific sensor or task, these embeddings provide compact semantic representations of land-surface conditions at a standardized spatial resolution [2,23]. Their global coverage and accessibility through Google Earth Engine make them potentially valuable for geological applications in which labeled samples are limited [23,24]. Nevertheless, the geological information contained in AEF embeddings has not been systematically evaluated. In particular, it remains unclear whether AEF can distinguish lithological units independently, whether it complements diagnostic hyperspectral information, and whether the resulting feature representation can support classification beyond the region used for model training.

Although conventional hyperspectral and machine learning approaches have improved lithological classification, distinguishing spectrally similar rock units and maintaining classification performance across different regions remain challenging. AEF embeddings provide complementary spatial and environmental information learned from multi-source and multi-temporal observations, which may improve the discrimination of spectrally similar lithological units. To address these questions, this study develops and evaluates a lithological classification framework that integrates AEF embeddings with features derived from GF-5 hyperspectral imagery. The hyperspectral variables include representative absorption bands, mineral-sensitive band-ratio indices, and spectral absorption parameters. Their classification performance is evaluated independently and in combination with AEF using RF and SVM classifiers. Rather than treating feature fusion as universally beneficial, we examine how its effectiveness depends on the structure of the feature space and the selected classifier. The influence of training sample size is also assessed, and a direct sample-transfer experiment is conducted across three adjacent mining areas to evaluate the spatial applicability of the derived feature relationships.

2. Data and Methods

2.1. Datasets

The study area, Bu'erkesitai, is located in the core of the Tangbale-Hatu metallogenic belt, in the northwestern Junggar Basin, representing a key segment of the Western Junggar gold-copper metallogenic province. The region is characterized by low-to-

https://doi.org/10.3390/min16121223

moderate relief and a clear northwest-to-southeast topographic gradient, with well-developed ridges, valleys, and gullies controlled by regional tectonics and long-term erosion. Bedrock weathering is intense and dominated by physical processes under an arid climate [25–27]. Sparse vegetation and strong tectonic fragmentation result in bedrock outcrop ratios exceeding 60%, especially within fault zones and intrusive contact zones. These characteristics provide excellent natural conditions for remote sensing-based lithological mapping, structural interpretation, and alteration extraction [28].

2.1.1. GF-5 Hyperspectral Imagery

GF-5 hyperspectral imagery was utilized as the core data source for lithological classification. GF-5 is China's first civilian hyperspectral satellite, acquiring observations covering a 0.40–2.50 μm spectral range with 330 bands, a 30 m spatial resolution, and a 60 km swath, enabling fine characterization of rock-forming minerals and alteration features. GF-5 Level-1 hyperspectral imagery acquired on 5 October 2024 was used in this study. Preprocessing included band screening, radiometric calibration, atmospheric correction using the Quick Atmospheric Correction (QUAC) module, geometric correction, and low-pass filtering, all performed in ENVI 5.6. Overlapping bands between the visible–near-infrared and shortwave-infrared ranges (151–154), invalid bands with zero DN values (192–199 and 246–261), and bands with low signal-to-noise ratios (325–330) were removed. The remaining bands were retained for subsequent processing. Radiometric calibration was applied to convert the original DN values to at-sensor radiance, followed by atmospheric correction using the Quick Atmospheric Correction (QUAC) module to get surface spectral reflectance, which was used for subsequent spectral feature extraction and analysis. Supporting datasets include 1:250,000-scale geological maps and 1000 field-verified lithological samples serving as ground truth for model training and validation [29]. All auxiliary geographic and geological data were obtained from the Geological Cloud Platform (https://geocloudsso.cgs.gov.cn, accessed on 1 June 2026). From the preprocessed GF-5 data, a suite of multi-feature components was extracted, including representative spectral bands, mineralization indices, and diagnostic absorption features [30]. The geographical extent of the study area is shown in Figure 1.

2.1.2. AEF Embeddings

To investigate the potential of remote sensing foundation-model representations for geological applications, AEF embeddings were introduced as an additional feature source. It provides globally consistent 64-dimensional embeddings generated through large-scale pretraining using multi-source Earth observation data and environmental information. Compared with manually designed spectral variables, AEF embeddings provide compact semantic representations that integrate broader land-surface characteristics [31]. The 2024 annual AEF embeddings were extracted for the study area from the Google Earth Engine collection at their native spatial resolution of 10 m and subsequently resampled to 50 m. Their classification performance was first evaluated separately and subsequently compared with hyperspectral features and fused feature combinations [2,32]. The purpose of introducing AEF was not to replace hyperspectral mineral information but to examine whether foundation-model representations provide complementary information for lithological discrimination under limited sample conditions.

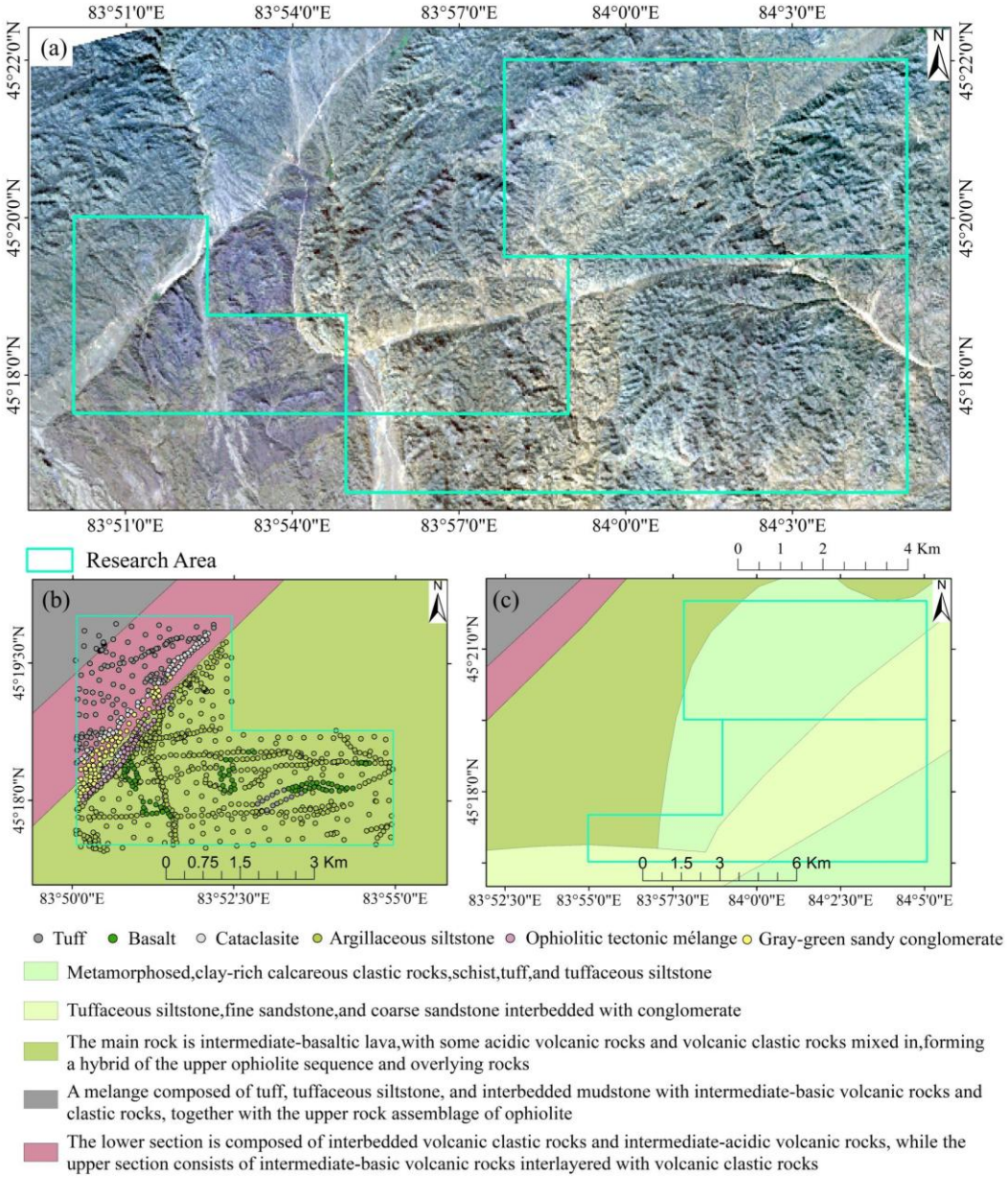


Figure 1. The Extent of the Study Area. (**a**) Study area extent and surface landforms in the GF-5 true-color composite. (**b**) Lithological map of the source area with sampling locations. (**c**) Spatial distribution of major lithological units in the target areas for cross-regional transfer.

2.1.3. Lithological Samples and Dataset Construction

Lithological samples were collected through field geological surveys with reference to existing geological information. Each georeferenced sample was assigned to its dominant lithological class and used as reference data for supervised classification. Because synchronous in situ hyperspectral measurements were not collected during the field survey, the spectral and feature values of each sample were extracted from the corresponding GF-5 image pixels at its geographic location. Differences in the spatial extent and accessibility of lithological outcrops resulted in unequal sampling opportunities and sample numbers among classes. The approximately 1000 field samples were divided into 700 training samples and 300 independent testing samples (Table 1). The training samples were used to construct the classification models, whereas the testing samples were used for accuracy assessment. Despite the overall sample size, several

lithological classes contained only 39–64 training samples, indicating that the available training data remained limited at the class level.

Table 1. Lithological classification samples.

ID	Lithology	Training Samples	Testing Samples
1	Tuff	97	41
2	Ophiolitic tectonic mélange	39	16
3	Argillaceous siltstone	378	163
4	Gray-green sandy conglomerate	70	30
5	Basalt	64	28
6	Cataclasite	51	22

2.2. Methodology

2.2.1. Feature Extraction of Hyperspectral Data

Differences in mineral composition primarily control variations in lithology. Diagnostic absorption features arising from electronic processes involving iron and vibrational processes associated with hydroxyl and carbonate groups provide important information for identifying rock-forming and alteration minerals. Different lithological classes may share similar mineral components; therefore, distinguishing them often requires considering the combined variations in multiple spectral features. Based on a literature review, 81 spectral features were integrated into multi-source feature-fusion datasets, including typical absorption bands, band-ratio features, and spectral absorption features [33]. In addition, the AEF feature set is briefly introduced. The detailed formulations of these features are provided in Table 2.

Table 2. Feature Extraction from Hyperspectral Data.

Feature Group	Feature Name	Calculation Method	Corresponding Central Wavelengths (nm)
Typical Absorption Bands	Selected absorption-band reflectance	B15, B16, B27, B28, B113, B114, B120, B121, B144, B145, B165, B177, B224, B225, B286, B287, B288, B289, B290, B291, B292, B301, B302, B303, B304, B305, B306, B307, B308, B309, B310, B311, B312, B313, B314, B325, B326	$\lambda_{447.22}$, $\lambda_{451.55}$, $\lambda_{498.66}$, $\lambda_{502.94}$, $\lambda_{867.29}$, $\lambda_{871.58}$, $\lambda_{897.30}$, $\lambda_{901.58}$, $\lambda_{1000.17}$, $\lambda_{1004.46}$, $\lambda_{1148.8101}$, $\lambda_{1249.8101}$, $\lambda_{1645.40}$, $\lambda_{1653.8101}$, $\lambda_{2167.23}$, $\lambda_{2175.6499}$, $\lambda_{2184.0701}$, $\lambda_{2192.48}$, $\lambda_{2200.8999}$, $\lambda_{2209.3201}$, $\lambda_{2217.73}$, $\lambda_{2293.48}$, $\lambda_{2301.8999}$, $\lambda_{2310.3201}$, $\lambda_{2318.73}$, $\lambda_{2327.1499}$, $\lambda_{2335.5701}$, $\lambda_{2343.98}$, $\lambda_{2352.3999}$, $\lambda_{2360.8201}$, $\lambda_{2369.23}$, $\lambda_{22,377.6499}$, $\lambda_{2386.0701}$, $\lambda_{2394.48}$, $\lambda_{2402.8999}$, $\lambda_{2495.48}$, $\lambda_{2503.8999}$
Band-Ratio features	Ferric iron (Fe^{3+})-related alteration	B65/B36	$\lambda_{661.54}/\lambda_{537.23}$
	Kaolinite–sericite alteration	B225/B291	$\lambda_{1653.81}/\lambda_{2209.32}$
	Kaolinite alteration	B225/B286	$\lambda_{1653.81}/\lambda_{2167.23}$
	Iron-bearing silicate alteration	B286/B225	$\lambda_{2167.23}/\lambda_{1653.81}$
	Sericitization (sericite alteration)	B286/B291	$\lambda_{2167.23}/\lambda_{2209.32}$
	Dolomite alteration	B286/B297	$\lambda_{2167.23}/\lambda_{2259.82}$
	Chloritization (chlorite alteration)	B306/B225	$\lambda_{2335.57}/\lambda_{1653.81}$
	Carbonate–chlorite–epidote alteration assemblage	(B297 + B312)/B306	$(\lambda_{2259.82} + \lambda_{2386.07})/\lambda_{2335.57}$

	Muscovite–kaolinite–alunite–illite/smectite alteration assemblage	(B286 + B297)/B291	$(\lambda_{2167.23} + \lambda_{2259.82})/\lambda_{2209.32}$
	Ferric iron (Fe^{2+})-related alteration	(B286/B99) + (B65/B36)	$(\lambda_{2167.23}/\lambda_{807.28}) + (\lambda_{661.54}/\lambda_{537.23})$
	Iron oxide alteration	B225/B99, (B65 + B99)/B36	$\lambda_{1653.81}/\lambda_{807.28}$ and $(\lambda_{661.54} + \lambda_{807.28})/\lambda_{537.23}$
	Gossan (iron cap) alteration	(B225/B99) + (B65/B36)	$(\lambda_{1653.81}/\lambda_{807.28}) + (\lambda_{661.54}/\lambda_{537.23})$
	Chlorite–epidote–amphibole alteration assemblage	(B291 + B312)/(B297 + B306)	$(\lambda_{2209.32} + \lambda_{2386.07})/(\lambda_{2259.82} + \lambda_{2335.57})$
	Muscovite–kaolinite–alunite–illite/smectite alteration assemblage	(B286 + B297)/B291	$(\lambda_{2167.23} + \lambda_{2259.82})/\lambda_{2209.32}$
Spectral Absorption Features	Absorption position (P)	$P = \lambda_{\max absorption}$	——
	Absorption depth (h)	$h = \lambda_base(P) - \lambda(P)$	
	Absorption width (w_1)	$w1 = \lambda_\lambda - \lambda_L$	
	Absorption area ($S_1 + S_2$)	$S = S_1 + S_2$	
	Absorption asymmetry (S_1/S_2)	$A = S_1/S_2$	
	full width at half maximum (FWHM, w_2)	$w_2 = \lambda_{\lambda,1/2} - \lambda_{L,1/2}$	

2.2.2. Feature Fusion

Feature fusion was performed by concatenating AEF embeddings with selected hyperspectral feature groups. Before fusion, the 37 band features, 14 band-ratio features, and spectral absorption parameters derived from GF-5 imagery were separately normalized to the range of 0–1. AEF embeddings were used in their native unit-length representation without additional normalization. During feature fusion, the GF-5 hyperspectral features were resampled to 50 m and spatially aligned with the 50 m AEF embeddings prior to feature concatenation. The objective of feature fusion was to evaluate whether global semantic representations from AEF could complement mineral-sensitive hyperspectral information. Different combinations were constructed, including hyperspectral features only, AEF features only, AEF combined with individual hyperspectral feature groups and AEF combined with multiple hyperspectral features. Because different classifiers respond differently to feature dimensionality and feature distribution, both RF and SVM were employed to evaluate the stability of different fusion strategies [33,34].

2.2.3. Classification Algorithms

RF and SVM are two widely validated machine learning classifiers that have demonstrated strong performance in remote sensing image classification tasks. RF was selected because of its robustness to nonlinear relationships, high-dimensional features, and limited training samples. RF constructs multiple decision trees using bootstrap sampling and random feature selection, and the final prediction is determined by ensemble voting. In this study, RF was used to evaluate whether different feature representations improved lithological separability under nonlinear classification conditions [12,33]. SVM was selected as another representative classifier because of its effectiveness in small-sample and high-dimensional classification problems. A radial basis function kernel was adopted to capture nonlinear boundaries among lithological classes. The SVM classifier was used to evaluate whether different feature representations provided stable class separation in feature spaces with limited samples [33,35,36].

2.2.4. Accuracy Assessment

To quantitatively evaluate the classification accuracy of the lithological results, a confusion matrix was employed for accuracy assessment. Overall Accuracy (OA) and the Kappa coefficient were used as evaluation metrics, and their definitions are given as follows.

$$\mathrm{OA} = \frac{\sum_{i=1}^{m} x_{ii}}{n} \times 100\% \tag{1}$$

$$\mathrm{Kappa} = \frac{n\sum_{i=1}^{m} x_{ii} - \sum_{i=1}^{m}(x_{i+}x_{+i})}{n^2 - \sum_{i=1}^{m}(x_i + x_{+i})} \tag{2}$$

In Equation (1), n denotes the total number of classes, and m represents the number of validation sample types; x_ii indicates the number of correctly classified samples. In Equation (2), m denotes the number of rows in the confusion matrix. x_{ii} represents the number of observations in the i-th row and i-th column. x_{i+} and x_{+i} denote the total number of samples in the i-th row and i-th column, respectively, while n is the total number of observations.

Considering the unequal sample sizes among the lithological classes, class-specific precision, recall, and F1-score were additionally calculated.

$$Precision_i = \frac{TP_i}{TP_i + FP_i} \tag{3}$$

$$Recall_i = \frac{TP_i}{TP_i + FN_i} \tag{4}$$

$$F1_i = \frac{2 \times Precision_i \times Recall_i}{Precision_i + Recall_i} \tag{5}$$

$$Balanced\ Accuracy = \frac{1}{C}\sum_{i=1}^{C} Recall_i \tag{6}$$

In Equations (3)–(6), TP_i, FP_i, and FN_i denote the numbers of true positives, false positives, and false negatives for the i-th lithological class, respectively. $\mathrm{Precision_i}$, $Recall_i$, and $F1_i$ represent the precision, recall, and F1-score of the i-th class, respectively, while (C) denotes the total number of lithological classes.

The feature consistency of the same lithological classes between the source and target areas was further evaluated using the coefficient of determination (R^2), Root Mean Square Error (RMSE), and Mean Absolute Error (MAE). The corresponding formulations are given as follows.

$$RMSE = \sqrt{\frac{1}{n}\sum_{i=1}^{n}(y_i - \hat{y}_i)^2} \tag{7}$$

$$MAE = \frac{1}{n}\sum_{i=1}^{n}|y_i - \hat{y}_i| \tag{8}$$

$$R^2 = 1 - \frac{\sum_{i=1}^{n}(y_i - \hat{y}_i)^2}{\sum_{i=1}^{n}(y_i - \bar{y}_i)^2} \tag{9}$$

In Equations (7)–(9), n denotes the number of selected fused bands; y_i represents the mean spectral value of the source region at the i-th band; $\hat{y}_i$ denotes the corresponding

mean feature value of the target region; and $\bar{y}_i$ represents the mean of the source-region spectral values across the selected bands.

3. Results

3.1. Contribution of Hyperspectral Feature Representations

To evaluate the discriminative capability of different hyperspectral representations, three individual feature groups, including typical absorption bands, band-ratio indices, and spectral absorption parameters, together with their fused feature set, were evaluated using both RF and SVM classifiers. The classification accuracies are summarized in Figure 2.

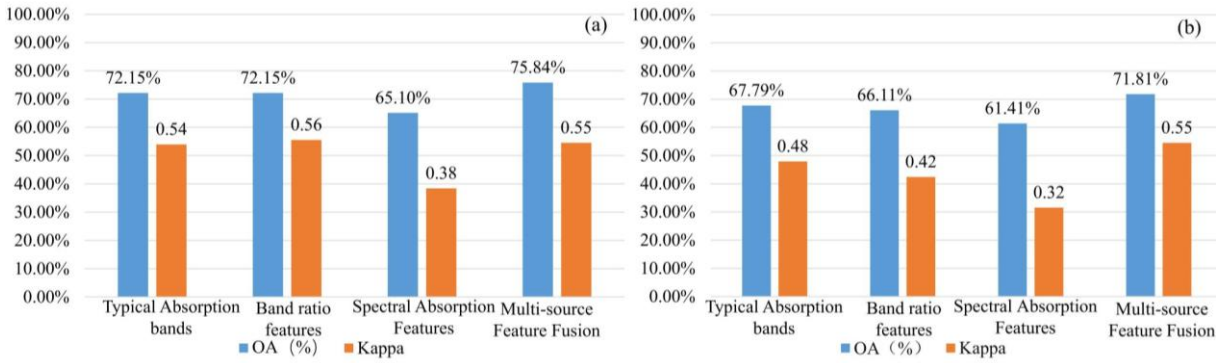


Figure 2. Performance of Different Hyperspectral Feature Sets. (**a**) RF; (**b**) SVM.

The classification performance varied considerably among feature representations. For both classifiers, the multi-source hyperspectral feature set consistently achieved the highest overall accuracy, reaching 75.84% (Kappa = 0.55) for RF and 71.81% (Kappa = 0.55) for SVM. In comparison, typical absorption bands and band-ratio indices produced intermediate accuracies, whereas spectral absorption parameters yielded the lowest performance under both classifiers. These results indicate that no individual spectral representation was sufficient to characterize lithological variability across the study area. Instead, combining complementary hyperspectral features substantially improved lithological discrimination by integrating mineral-sensitive spectral information from multiple perspectives.

The classification maps shown in Figures 3 and 4 further support this observation. Classifications derived from individual feature groups exhibited fragmented lithological boundaries and local misclassification, particularly in transitional zones between adjacent rock units. In contrast, the fused hyperspectral feature set generated more spatially continuous lithological distributions with clearer class boundaries, indicating that feature fusion enhanced the stability of spatial prediction in addition to improving overall classification accuracy.

These results demonstrate that the complementary information contained in different hyperspectral feature groups contributes more to lithological discrimination than any single spectral representation alone, providing a stronger spectral basis for subsequent feature-fusion experiments with AEF embeddings.

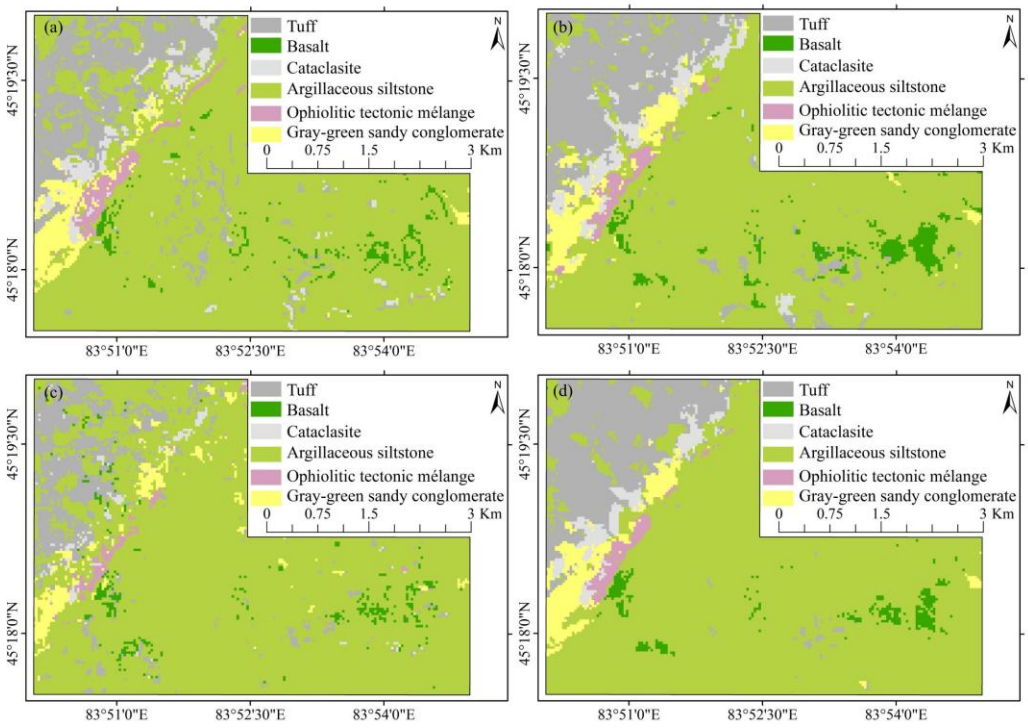


Figure 3. Classification results for RF with different hyperspectral characteristics. (**a**) Typical absorption bands. (**b**) Ratio features. (**c**) Spectral absorption features. (**d**) Multi-source feature fusion.

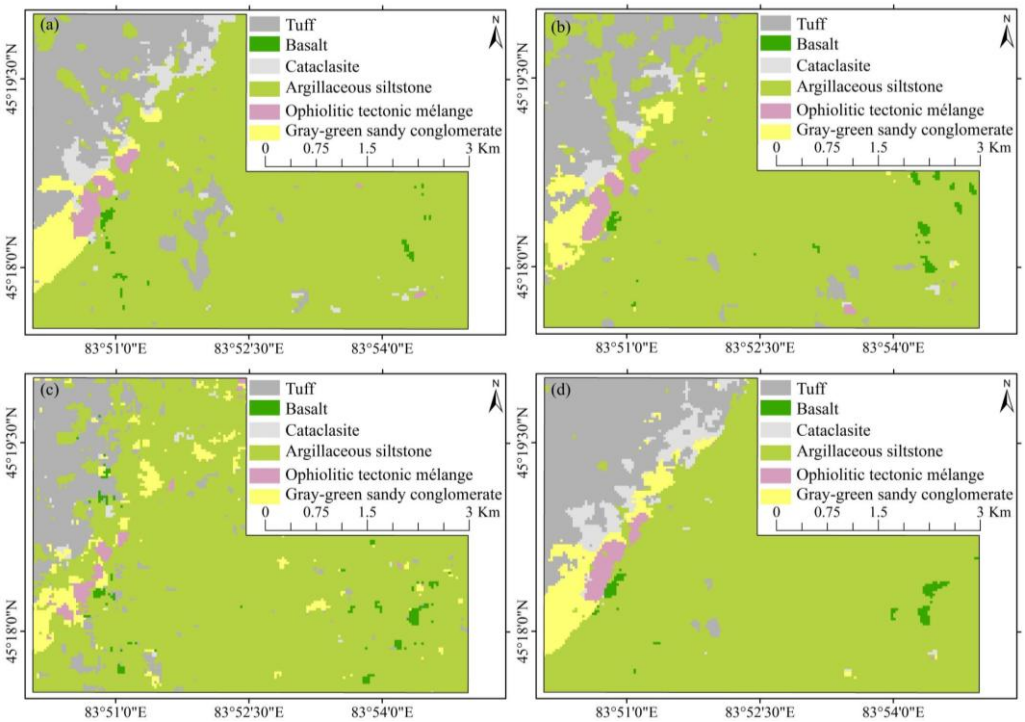


Figure 4. Classification results for SVM with different hyperspectral characteristics. (**a**) Typical absorption bands. (**b**) Ratio features. (**c**) Spectral absorption features. (**d**) Multi-source feature fusion.

3.2. Performance of AEF Embedding with Sample Size Variation

To investigate the influence of training sample availability, RF and SVM classifiers were applied to both the fused hyperspectral feature set and the AEF embeddings under different sample sizes. Training subsets ranging from 100 to 700 samples at intervals of 100 were constructed. All models were evaluated using the same independent testing

dataset to ensure comparability of classification performance. The corresponding results are presented in Figure 5. For both datasets, classification accuracy increased with the number of training samples and gradually stabilized when all available samples were used, indicating that additional training samples primarily improved model performance during the early stages of learning. Using the fused hyperspectral features, RF consistently outperformed SVM across all sample sizes, achieving a maximum overall accuracy of 75.84%, compared with 71.81% for SVM. This result suggests that RF provided more robust classification performance for conventional hyperspectral feature representations.

A different trend was observed for the AEF embeddings. Both classifiers achieved higher classification accuracies than those obtained using the hyperspectral feature set alone. When all samples were used, RF achieved an overall accuracy of 76.33%, whereas SVM reached 78.00%, representing the highest classification accuracy among all single-feature experiments. Across the reduced training subsets of 100–600 samples, AEF achieved overall accuracies ranging from 68.30% to 77.00% with RF and from 69.67% to 76.67% with SVM. Unlike the hyperspectral feature set, where RF consistently performed better, AEF embeddings produced slightly higher accuracy with SVM, indicating that the pretrained embedding space was more compatible with the nonlinear decision boundary constructed by SVM. These results indicate that AEF embeddings provide a highly discriminative feature representation for lithological classification. Moreover, the classification performance achieved with reduced training subsets suggests that the pretrained semantic representations retain useful geological information even under relatively limited training data.

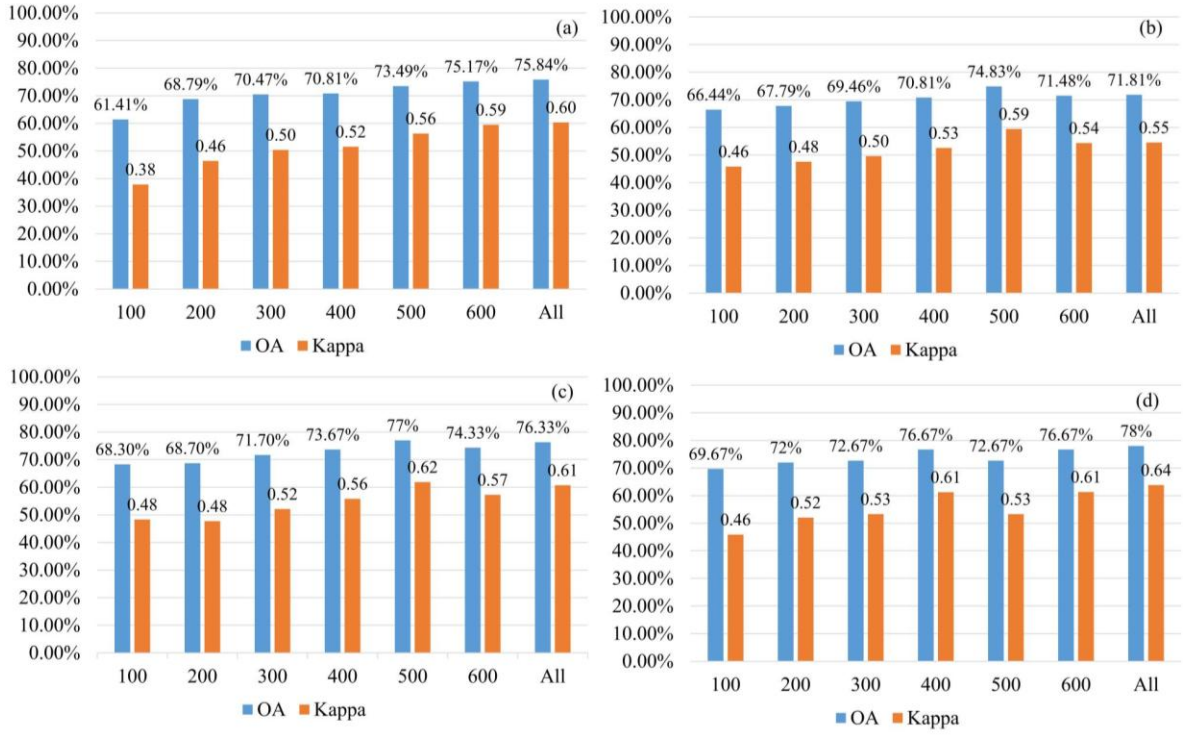


Figure 5. Classification accuracy based on Hyperspectral features and AEF embedding. (**a**) RF with Hyperspectral Features. (**b**) SVM with Hyperspectral Features. (**c**) RF with AEF. (**d**) SVM with AEF.

3.3. Effects of AEF-Hyperspectral Feature Fusion

To further evaluate whether AEF embeddings provide complementary information to hyperspectral features, AEF was combined with different hyperspectral feature groups, including typical absorption bands, band-ratio indices, spectral absorption parameters,

and the fused hyperspectral feature set. The classification results are summarized in Tables 3 and 4.

Table 3. Effects of AEF Feature Fusion on Classification Accuracy.

Method	Features	OA (%) [95% CI]	Kappa
RF	AEF	76.3 [71.21, 80.79]	0.607
	AEF+ multi-source feature fusion	78.0 [72.97, 82.32]	0.637
	AEF+ typical absorption bands	77.0 [71.91, 81.40]	0.613
	AEF+ Ratio indices	79.3 [74.39, 83.53]	0.656
	AEF+ spectral absorption features	75.3 [70.16, 79.87]	0.587
SVM	AEF	78.0 [72.97, 82.32]	0.638
	AEF+ multi-source feature fusion	77.7 [72.62, 82.01]	0.640
	AEF+ typical absorption bands	57.3 [51.68, 62.80]	0.105
	AEF+ Ratio indices	78.0 [72.97, 82.32]	0.637
	AEF+ spectral absorption features	47.7 [42.08, 53.31]	0.153

Table 4. Classification performance and statistical comparison.

Classifier	Comparison	ΔOA (pp) [95% CI]	McNemar *p*-Value
RF	AEF + multi-source features vs. AEF	1.67 [−2.20, 5.53]	0.500
	AEF + typical absorption bands vs. AEF	0.67 [−3.03, 4.37]	0.860
	AEF + band-ratio indices vs. AEF	3.00 [−0.86, 6.86]	0.175
	AEF + spectral absorption features vs. AEF	−1.00 [−4.87, 2.87]	0.736
SVM	AEF + multi-source feature fusion vs. AEF	−0.33 [−4.62, 3.96]	1.000
	AEF + band-ratio indices vs. AEF	0.00 [−3.34, 3.34]	1.000

The effectiveness of feature fusion differed markedly between RF and SVM. For RF, integrating AEF with most hyperspectral feature groups resulted in numerical improvements in classification accuracy relative to using AEF alone. Among all combinations, AEF + band-ratio indices achieved the highest performance, with an overall accuracy of 79.3% and a Kappa coefficient of 0.656, representing the best classification result obtained in this study. Fusion with the complete hyperspectral feature set and with typical absorption bands also improved classification accuracy, whereas combining AEF with spectral absorption parameters resulted in a slight reduction in performance. In contrast, SVM exhibited a substantially different response to feature fusion. AEF alone already achieved high classification accuracy (78.0%, Kappa = 0.638), and integrating multi-source hyperspectral features or band-ratio indices produced only marginal changes. However, incorporating typical absorption bands or spectral absorption parameters caused a pronounced decrease in classification performance, reducing overall accuracy to 57.3% and 47.7%, respectively.

The class-specific results presented in Table 5 further revealed substantial differences in classification performance among the lithological classes. Although RF and SVM using AEF + band-ratio indices achieved relatively high overall accuracies, their balanced accuracies were only 59.40% and 56.32%, respectively. Both models performed relatively well for tuff, argillaceous siltstone, and gray-green sandy conglomerate, but showed lower F1-scores for ophiolitic tectonic mélange and basalt. In particular, RF correctly identified only 2 of the 28 basalt samples, resulting in a recall of 7.14% and an F1-score of 13.33%, despite a precision of 100.00%. The SVM model failed to correctly identify any basalt samples. These results indicate that the relatively high overall accuracies did not correspond to uniformly high classification performance across all lithological classes.

Table 5. Class-specific performance of the AEF and band-ratio feature configuration.

Classifier and Feature Configuration	Lithological Class	Testing Samples	Precision (%)	Recall (%)	F1-Score (%)
RF: AEF + band-ratio indices	Tuff	41	94.12	78.05	85.33
	Ophiolitic tectonic mélange	16	55.56	31.25	40.00
	Argillaceous siltstone	163	79.70	98.77	88.22
	Gray-green sandy conglomerate	30	76.47	86.67	81.25
	Basalt	28	100.00	7.14	13.33
	Cataclasite	22	63.16	54.55	58.54
SVM: AEF + band-ratio indices	Tuff	41	85.71	87.80	86.74
	Ophiolitic tectonic mélange	16	44.44	25.00	32.00
	Argillaceous siltstone	163	80.71	97.55	88.33
	Gray-green sandy conglomerate	30	66.67	86.67	75.36
	Basalt	28	0.00	0.00	0.00
	Cataclasite	22	69.23	40.90	51.43

Overall, these results demonstrate that the contribution of AEF depends not only on the complementary information provided by hyperspectral features but also on the classifier used for feature learning. While RF generally achieved higher observed accuracies with several heterogeneous feature combinations, SVM exhibited greater sensitivity to feature composition, indicating that the effectiveness of feature fusion is classifier-dependent rather than universally beneficial.

3.4. Cross-Regional Consistency of Lithological Features

The mean spectral reflectance of unconsolidated sediments, ophiolitic tectonic melange, metamorphosed clastic rocks and basalt derived from the QUAC-corrected GF-5 image at source and target sample locations are shown in Figure 6. They were used to build normalized 81-dimensional feature vectors. To further evaluate the cross-regional consistency of lithological features at the class level, the mean multi-source feature vectors of individual lithological units in the source and target areas were compared using R^2, RMSE, and MAE (Table 6, Figures 7 and 8). The cross-regional consistency of feature representations varied considerably among lithological units, indicating that the stability of the evaluated features was lithology-dependent rather than uniform across all classes. Lithological units characterized by relatively homogeneous mineral compositions and spectral responses may exhibit greater consistency between the source and target areas. In contrast, units exhibiting heterogeneous mineral assemblages or gradual lithological transitions may show larger differences in feature representations across regions.

Compared with hyperspectral features alone, the incorporation of AEF embeddings generally improved the separability of several lithological classes, particularly for units that exhibited relatively weak spectral contrast. The improvements were reflected not only in higher overall accuracy but also in the reduction in inter-class confusion, suggesting that the semantic information contained in AEF complements the mineral-sensitive information derived from hyperspectral imagery.

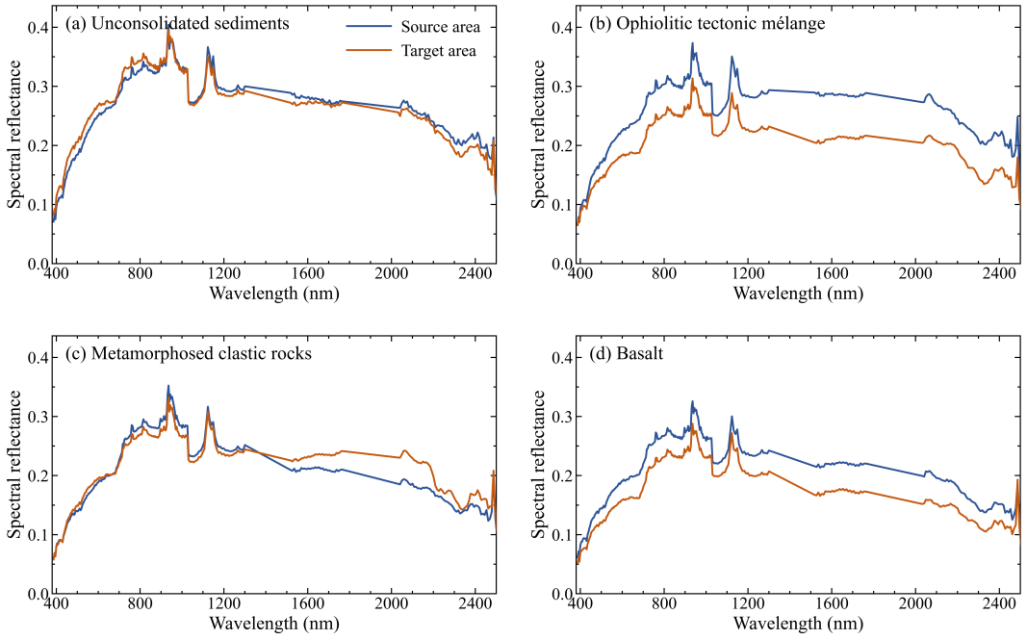


Figure 6. Mean surface spectral reflectance of representative lithological types in the source and target areas. (**a**) Unconsolidated sediments; (**b**) Ophiolitic tectonic mélange; (**c**) Metamorphosed clastic rocks; (**d**) Basalt.

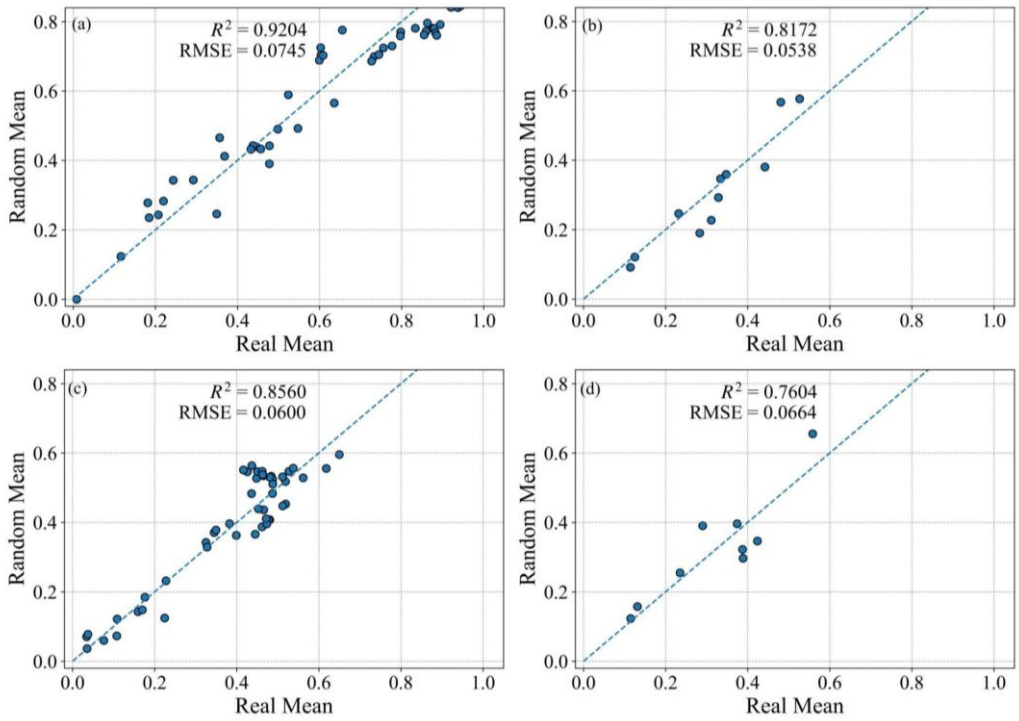


Figure 7. Coefficient of determination (R^2) for different lithological types. (**a**) Unconsolidated sediments. (**b**) Ophiolitic tectonic mélange. (**c**) Metamorphosed clastic rocks. (**d**) Basalt.

https://doi.org/10.3390/min16121223

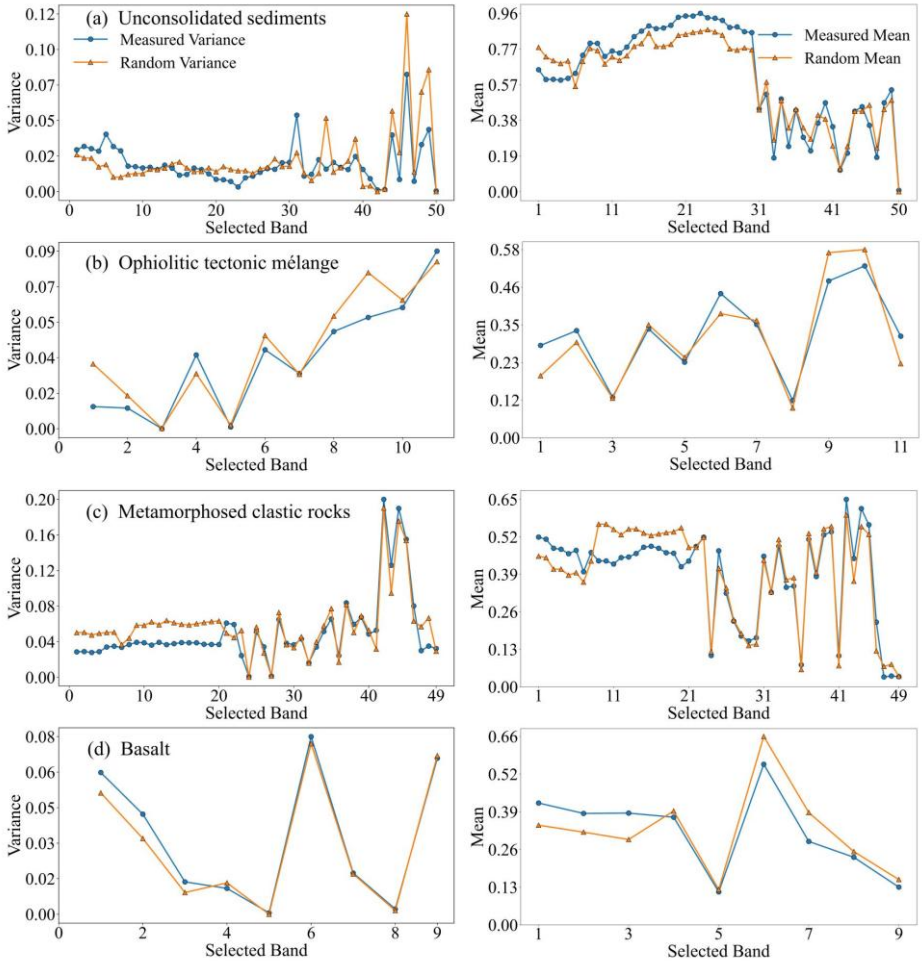


Figure 8. Variance and mean feature curves of different lithological types in the source and target areas. (**a**) Unconsolidated sediments. (**b**) Ophiolitic tectonic mélange. (**c**) Metamorphosed clastic rocks. (**d**) Basalt.

Nevertheless, improvements were not uniform across all lithological categories. Several structurally complex or spectrally similar units remained difficult to distinguish regardless of the feature configuration. This observation indicates that classification uncertainty was primarily associated with intrinsic geological similarity rather than insufficient feature dimensionality. Consequently, the effectiveness of feature fusion depended on the spectral characteristics of individual lithological units instead of producing a uniform improvement for every class.

Overall, the class-level evaluation demonstrates that integrating AEF embeddings with hyperspectral features enhances lithological discrimination for multiple rock units while maintaining stable classification performance across the entire study area. However, the degree of improvement varies according to the spectral and geological characteristics of individual lithologies.

Table 6. Cross-regional consistency assessment of lithological features.

Lithology	R^2	RMSE	MAE
Unconsolidated sediments	0.9204	0.0745	0.0656
Ophiolitic tectonic mélange	0.8172	0.0538	0.0433
Metamorphosed clastic rocks	0.8560	0.06	0.0481
Basalt	0.7604	0.0664	0.0564

3.5. Cross-Regional Transferability

To evaluate the spatial applicability of the proposed feature representations, the classification model trained in the source mining area was directly transferred to adjacent mining regions without additional retraining. The corresponding classification maps are presented in Figure 9. The transferred classifications successfully reproduced the overall spatial distribution of the major lithological units in the target regions. Large-scale geological boundaries and the dominant lithological patterns remained spatially continuous, indicating that the learned feature representations retained a certain degree of generalization capability beyond the original training area.

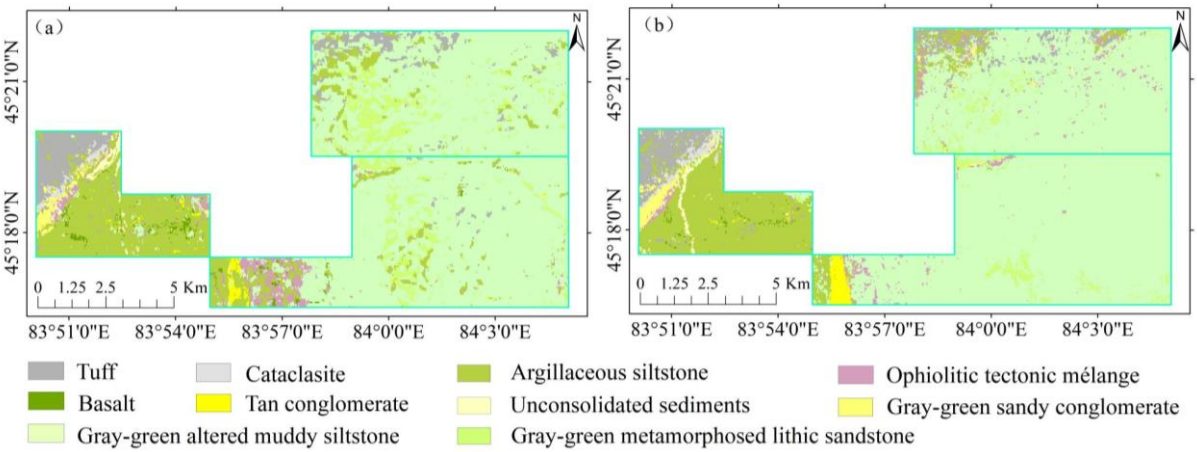


Figure 9. Results of the lithological classification of the sample. (**a**) Multi-source feature fusion; (**b**) AEF+ multi-source feature fusion.

Although the overall lithological distribution was well preserved, local differences remained in several structurally complex areas. Misclassification mainly occurred along lithological transition zones and in rock units exhibiting similar spectral characteristics. These local inconsistencies suggest that regional variations in geological background and surface conditions continue to influence classification performance after model transfer. Among the evaluated feature configurations, models incorporating AEF embeddings generally produced more coherent regional mapping results than those relying solely on hyperspectral features. The transferred classifications exhibited improved spatial continuity and reduced fragmentation in several lithological units, indicating that the pretrained semantic representations contributed useful regional information beyond local spectral characteristics.

The transfer experiment demonstrates that the proposed feature representation maintains reasonable classification capability across neighboring mining areas and provides a practical basis for reducing field sampling requirements in regional lithological mapping. At the same time, the remaining local discrepancies indicate that additional adaptation strategies may still be required when transferring models to geologically more heterogeneous regions.

4. Discussion

4.1. Advantages of AEF Embedding and Hyperspectral Features

The experimental results demonstrate that AEF embeddings and hyperspectral features provide complementary rather than redundant information for lithological classification. Hyperspectral imagery primarily captures mineral-related spectral absorption characteristics, enabling discrimination of lithological units with distinct

mineral compositions. It should be noted that VSWIR observations characterize exposed surface spectra, which may be modified by diagenesis, weathering, and secondary alteration, particularly in sedimentary rocks. Therefore, the mapped lithologies represent present-day surface spectral expressions rather than the pristine mineral composition of the parent rocks. However, its representation is largely limited to local spectral responses and is susceptible to spectral similarity caused by weathering, mixed pixels, and surface conditions. In contrast, the AEF embeddings achieved competitive classification accuracy even without hyperspectral inputs, indicating that the pretrained representations encode broader land-surface information relevant to lithological mapping. This difference suggests that the contribution of AEF may extend beyond mineral-sensitive spectral responses to include other surface characteristics associated with lithological variations. The geological relevance of the 64-dimensional AEF embeddings can be understood through the influence of lithological and mineralogical properties on remotely sensed surface characteristics. Variations in mineral composition, weathering intensity, hydrothermal alteration, and geomorphological conditions can produce differences in surface reflectance, texture, and spatial patterns. By integrating multi-source and multi-temporal Earth observation information, AEF embeddings may capture these geologically relevant variations within a compact feature space [23]. Previous research has demonstrated the applicability of AEF embeddings to lithological classification and the extraction of mineral alteration-related information, providing further evidence of their potential to capture geologically meaningful surface patterns [37]. Nevertheless, the 64 embedding dimensions are learned latent features rather than physically defined mineralogical parameters. Therefore, the relationships between individual embedding dimensions and specific minerals or diagnostic absorption features remain unclear and require further validation.

The fusion experiments further suggest that the contribution of AEF is not simply an increase in feature dimensionality. Instead, AEF provides additional semantic information that complements the mineral-sensitive characteristics extracted from hyperspectral imagery. Consequently, feature fusion improved the discrimination of several lithological units, particularly those exhibiting weak spectral contrast or complex geological settings. These findings indicate that foundation-model embeddings can serve as a complementary feature source for geological remote sensing rather than replacing conventional hyperspectral observations.

4.2. Implications of Foundation Models for Lithological Mapping

Recent remote sensing foundation models have demonstrated considerable potential in land-cover mapping and environmental monitoring [38]. However, their application to geological remote sensing remains limited. The present study provides one of the first systematic evaluations of AEF embeddings for lithological classification using hyperspectral imagery. The results demonstrate that pretrained embeddings contain transferable information relevant to geological discrimination and remain effective under different training sample sizes and cross-regional transfer experiments.

These findings suggest that foundation models may provide a new representation paradigm for geological mapping. Instead of relying exclusively on manually designed spectral indices or mineral-sensitive absorption features, future lithological classification frameworks may combine physically interpretable hyperspectral variables with pretrained semantic representations to improve robustness and transferability. Such a strategy is particularly attractive in regions where field observations are limited or where labeled geological samples are difficult to obtain.

Nevertheless, the results also indicate that foundation-model embeddings should be regarded as complementary rather than independent geological descriptors. Their

contribution depends on the geological characteristics of the study area, the selected hyperspectral features, and the classification algorithm. Although combining AEF with band-ratio indices produced the highest observed OA, the improvement over AEF alone was not statistically significant. This result therefore indicates a numerical advantage rather than a demonstrated improvement in predictive performance. Consequently, integrating domain-specific geological knowledge with foundation-model representations is likely to be a more effective direction than replacing conventional spectral analysis entirely.

4.3. Limitations and Future Work

Although the proposed framework achieved encouraging classification performance, several limitations remain. First, the class-specific evaluation was limited by sample imbalance and mixed lithological conditions. Some boundary samples contained multiple lithological components but were assigned a single dominant class for supervised classification. This mismatch between reference labels and mixed spectral responses may have increased class confusion, resulting in lower recall and F1-scores for some classes. Future studies should increase minority-class samples and distinguish samples within lithological units from mixed boundary samples. Second, the evaluation was conducted using one GF-5 hyperspectral dataset and three adjacent mining areas. The transferability of AEF embeddings under substantially different geological environments has not yet been fully investigated. Future studies should evaluate the proposed framework across broader geological settings with greater lithological diversity. Third, the current feature fusion strategy adopts direct feature concatenation after resampling and spatially aligning AEF embeddings and GF-5 hyperspectral features to a common 50 m grid. This spatial harmonization may result in some loss of spatial detail. More advanced fusion approaches, such as feature alignment, representation disentanglement, or attention-based fusion, may further improve the integration of hyperspectral and foundation-model representations while reducing feature redundancy. Finally, this study focuses on supervised lithological classification. **T**he RF and SVM classifiers used in this study are data-driven models that learn statistical relationships between the input features and lithological labels rather than explicitly resolving the underlying mineralogical mechanisms. Further integration of field spectroscopy and mineralogical measurements is required to improve the physical interpretation of the classification results. As foundation models continue to evolve, integrating pretrained representations with geological prior knowledge, self-supervised learning, and domain adaptation techniques may further improve the generalization capability of geological remote sensing models under limited-sample conditions.

5. Conclusions

Accurate lithological classification remains challenging because hyperspectral spectral variability, limited training samples, and regional geological heterogeneity collectively reduce the generalization capability of conventional remote sensing methods. To address these challenges, this study systematically evaluated the potential of AEF embeddings for lithological mapping by integrating pretrained semantic representations with GF-5 hyperspectral features. The proposed framework was comprehensively assessed using different feature combinations, two representative classifiers, varying training sample sizes, and cross-regional transfer experiments.

The main findings of this study can be summarized as follows.

(1) Different hyperspectral feature representations provide complementary lithological information. Multi-feature hyperspectral fusion consistently achieved higher

classification accuracy than individual spectral feature groups, indicating that integrating absorption bands, band-ratio indices, and spectral absorption parameters provides a more comprehensive description of lithological spectral characteristics than any single feature representation alone.

(2) AEF embeddings contain transferable information that complements hyperspectral observations rather than replacing them. AEF achieved competitive classification performance as an independent feature representation and further improved classification accuracy when combined with selected hyperspectral features. However, the contribution of AEF depended on the classifier and feature configuration, indicating that foundation-model representations should be regarded as complementary semantic information instead of universally superior geological descriptors.

(3) The effectiveness of feature fusion is classifier-dependent. RF generally achieved higher observed accuracies with several heterogeneous feature combinations, whereas SVM exhibited greater sensitivity to feature composition. This finding demonstrates that the performance of foundation-model feature fusion is governed not only by feature quality but also by the compatibility between feature representations and classification algorithms.

This study demonstrates that integrating pretrained foundation-model embeddings with mineral-sensitive hyperspectral features provides an effective strategy for lithological classification under limited-sample conditions. More importantly, the results suggest that foundation-model representations should be incorporated as complementary semantic features within geological remote sensing workflows rather than replacing conventional hyperspectral analysis. This study provides a practical reference for applying remote sensing foundation models to lithological mapping and offers insights into future geological classification frameworks that combine physically interpretable spectral information with pretrained geospatial representations.

Author Contributions: C.X. and P.Z. conceived and designed the research ideas; C.X., Y.L. and P.X. participated in the field investigation; C.X. and B.W. performed the data processing; and C.X., B.W. and L.C. reviewed and edited the draft. All the data were obtained from previous work performed by the project team. All authors have read and agreed to the published version of the manuscript.

Funding: This study was financially supported by the Shandong Provincial Natural Science Foundation (ZR2025QC416, ZR2026MS0544), the National Key Research and Development Program of China (2025YFE0109600), the National Natural Science Foundation of China (42177167, L2424330), and the Science and Technology Program of Guangzhou (2025A03J3171), and Science and technology project of Shandong Provincial Bureau of Geology and Mineral Resources (KY202502, HJ202505).

Data Availability Statement: The datasets presented in this article are not readily available because the data are part of an ongoing study. Requests to access the datasets should be directed to corresponding authors.

Conflicts of Interest: The authors declare no conflicts of interest.

References

1. Chen, T.Y. Research on Automatic Lithological Classification Methods Based on Remote Sensing. Master's Thesis, Jilin University, Changchun, China, 2025.
2. Hajaj, S.; Harti, A.E.; Jellouli, A.; Pour, A.B.; Himyari, S.M.; Hamzaoui, A.; Hashim, M. Evaluating the Performance of Machine Learning and Deep Learning Techniques to HyMap Imagery for Lithological Mapping in a Semi-Arid Region: Case Study from Western Anti-Atlas, Morocco. *Minerals* **2023**, *13*, 22.

3. Chen, L.; Wang, L.; Ma, Y.; Lin, Y.; Chen, S. Coupling normalized abundance with an improved continuum removal algorithm for quantitative inversion of carbonate minerals using hyperspectral data. *Ore Geol. Rev.* **2024**, *166*, 105927.
4. Chen, S.; Chen, L.; Liu, Y.; Li, X. Experimental simulation on mixed spectra of leaves and calcite for inversion of carbonate minerals from EO-1 Hyperion data. *GIScience Remote Sens.* **2013**, *50*, 690–703.
5. Hui, Z.; Wang, R.; Chen, W.; Zhou, G.; Li, J. Lithologic Unit Classification Attention-Based and Multiscale Geology Knowledge-Guided Framework in Vegetated Areas. *IEEE Trans. Geosci. Remote Sens.* **2025**, *63*, 4417715.
6. Ke, Y.; Shi, Z.; Li, P.; Zhang, X. Lithological classification and analysis based on Hyperion hyperspectral data and the Random Forest method. *Acta Petrol. Sin.* **2018**, *34*, 2181–2188.
7. Chi, Y.; Zhang, N.; Jin, L.; Liao, S.; Zhang, H.; Chen, L. Comparative Analysis of GF-5 and Sentinel-2A Fusion Methods for Lithological Classification: The Tuanjie Peak, Xinjiang Case Study. *Sensors* **2024**, *24*, 23.
8. Ying, Z.; Baozhi, P. Application of Various Lithologic Classification Methods to Volcanic Rock Identification. *Well Logging Technol.* **2011**, *5*, 474–478.
9. Abdul-Qadir, A.M. Supervised Classification for Lithologic Discrimination in Shaikh Ibrahim Area, NW Iraq Using Landsat Images. *Arab. J. Sci. Eng.* **2014**, *39*, 437–451.
10. Li, S.; Dong, Y.; Zhang, G. Study on automatic lithology identification based on convolutional neural network and deep transfer learning. *Discov. Appl. Sci.* **2024**, *6*, 1–16.
11. Zhu, M.; Li, B.; Fu, H.; Chen, C.; Gao, M. Lithological classification based on SVM using multi-source data synergy: A case study of the Jiangalasayi area. *Uranium Geol.* **2020**, *36*, 288–292, 317.
12. Kuhn, S.; Cracknell, M.J.; Reading, A.M. Lithologic mapping using Random Forests applied to geophysical and remote-sensing data: A demonstration study from the Eastern Goldfields of Australia. *Geophysics* **2018**, *83*, B183–B193.
13. Guo, D.; Wang, Z.; Zuo, R. Large-scale Himalayan Leucogranite Mapping Based on Multi-source Remote-Sensing Data and U-Net Convolutional Network. *Nat. Resour. Res.* **2025**, *34*, 2403–2421.
14. Ghoneim, S.M.; Wang, C.; Abdelrahman, K.; Ali, H.F. Mapping alteration zones at Kab Amiri area, Egypt: New insights from the EnMAP hyperspectral satellite data. *J. Afr. Earth Sci.* **2025**, *228*, 105666.
15. Ghoneim, S.M.; Wang, C.; Ali, H.F.; Yahaya, I.I.; Faisal, M. Machine learning-assisted hyperspectral targeting of orogenic and placer gold deposits at Wadi Umm Eish El-Zarqa, Egypt. *Min. Mineral. Depos.* **2026**, *20*, 10–22.
16. Zhang, H.; Yuan, C.; Zhao, L.; Shi, W.; Liu, J. Research on sedimentary rock classification based on infrared reflectance spectroscopy. *Acta Petrol. Mineral.* **2025**, *44*, 1257–1266.
17. Lu, J.; Han, L.; Zha, X.; Li, L. Lithology classification in semi-arid areas based on vegetation suppression integrating microwave and optical remote sensing images: Duolun county, Inner Mongolia autonomous region, China. *Geocarto Int.* **2022**, *37*, 25.
18. Guo, M. Automatic lithological classification of the sinian system based on spectral features and machine learning: A case study from the Gaozhu section in Wuxi. *Microchem. J.* **2025**, *218*, 115175.
19. Ibrahim, B.; Ahenkorah, I.; Ewusi, A.; Majeed, F. A novel XRF-based lithological classification in the Tarkwaian paleo placer formation using SMOTE-XGBoost. *J. Geochem. Explor.* **2023**, *245*, 107147.
20. Li, S.; Lin, P.; Xu, Z.; Xiang, H.; Li, Q. Intelligent lithological identification based on transfer learning of hyperspectral rock images. *Spectrosc. Spectr. Anal.* **2025**, *45*, 2289–2301.
21. Shebl, A.; Csamer, A. Stacked vector multi-source lithologic classification utilizing Machine Learning Algorithms: Data potentiality and dimensionality monitoring. *Remote Sens. Appl. Soc. Environ.* **2021**, *24*, 100643.
22. Zhang, Z.; Wang, G.; Carranza, E.J.M.; Yang, S.; Zhao, K.; Yang, W.; Sha, D. Three-Dimensional Pseudo-Lithologic Modeling Via Adaptive Feature Weighted k-Means Algorithm from Multi-Source Geophysical Datasets, Qingchengzi Pb–Zn–Ag–Au District, China. *Nat. Resour. Res.* **2022**, *31*, 2163–2179.
23. Brown, C.F.; Kazmierski, M.R.; Pasquarella, V.J.; Rucklidge, W.J.; Samsikova, M.; Zhang, C.; Shelhamer, E.; Lahera, E.; Wiles, O.; Ilyushchenko, S. AlphaEarth Foundations: An embedding field model for accurate and efficient global mapping from sparse label data. *arXiv* **2025**, arXiv:2507.22291.
24. Qin, Q. AlphaEarth Foundations: Potential and challenges of foundation models for remote sensing. *J. Geo-Inf. Sci.* **2025**, *27*, 2283–2290.
25. An, F.; Zhu, Y. Studies on geology and geochemistry of alteration-type ore in the Hatu gold deposit (Western Junggar), Xinjiang, NW China. *Mineral. Depos.* **2007**, *26*, 621.
26. Feng, L.; Yu, M.; Yang, B.; Zhang, D. Geologic features, ore-controlling factors and ore-prospecting indicators of the Bieluagaxi gold deposit, Tuoli County, Xinjiang. *Gold* **2017**, *38*, 15–18.

27. Zhang, C.; Huang, S.; Zhang, B.; Shen, Y.; Yalikun, Y.; Wang, J.; Shang, Y. Mineral prospectivity mapping based on remote sensing and machine learning in the Hatu area, China. *Minerals* **2026**, *16*, 144.
28. Yuan, H.; Li, A.; Huang, W.; Hu, Z.; Zuo, Y.; Yang, X. Geological deformation of the Tuoli Fault in the West Junggar since the Late Quaternary. *Seismol. Geol.* **2023**, *45*, 49–66.
29. Liu, Y.; Sun, D.; Hu, X.; Ye, X.; Li, Y.; Liu, S.; Cao, K.; Chai, M.; Zhou, W.; Zhang, J.; et al. The Advanced Hyperspectral Imager: Aboard China's GaoFen-5 satellite. *IEEE Geosci. Remote Sens. Mag.* **2019**, *7*, 23–32.
30. Van der Werff, H.; Van der Meer, F. Sentinel-2A MSI and Landsat 8 OLI provide data continuity for geological remote sensing. *Remote Sens.* **2016**, *8*, 883.
31. Alvarez, C.; Vaca, C.U.; Llumipanta, N.E. Machine learning for urban air quality prediction using Google AlphaEarth Foundations satellite embeddings: A case study of Quito, Ecuador. *Remote Sens.* **2025**, *17*, 3472.
32. Wang, W.; Guo, H.; He, S.; Qi, F.; Samat, A.; Wang, D.; Li, J. AI-driven precision mapping of tea plantations using AlphaEarth Foundations: A scalable solution for smart agricultural monitoring. *Agriculture* **2026**, *16*, 412.
33. Hu, L.; Lu, Y.; Gan, S.; Yuan, X.; Chen, C.; Zhu, Z. Spatial distribution of Lufeng Dinosaur Valley outcrops based on the GF-5 hyperspectral OS–SPA–SVM model. *J. Spectrosc.* **2025**, *2025*, 5547125.
34. Masoumi, F.; Eslamkish, T.; Abkar, A.A.; Honarmand, M.; Harris, J.R. Integration of spectral, thermal, and textural features of ASTER data using Random Forests classification for lithological mapping. *J. Afr. Earth Sci.* **2017**, *129*, 445–457.
35. Liu, H.; Huang, X.; Wang, W. Lithological mapping in plateau regions by integrating spectral feature selection and deep learning: A case study of the Gonjo area, Tibet. *Remote Sens.* **2026**, *18*, 1621.
36. Bachri, I.; Hakdaoui, M.; Raji, M.; Teodoro, A.C.; Benbouziane, A. Machine learning algorithms for automatic lithological mapping using remote sensing data: A case study from Souk Arbaa Sahel, Sidi Ifni Inlier, Western Anti-Atlas, Morocco. *ISPRS Int. J. Geo-Inf.* **2019**, *8*, 248.
37. Cheng, Q.; Yang, Y.; Zhou, Y.; Zhang, Y. Earth science in the era of foundation models: How AlphaEarth is reshaping quantitative geoscience. *Earth Sci. Front.* **2025**, *32*, 396–410.
38. Rojas-Lucero, J.; Solano-Correa, Y.; Kolarik, N.; Brandt, J.; Caughlin, T. Spectral indices outperform AlphaEarth foundation embeddings for aboveground biomass estimation in a regenerating tropical Andean forest. *Remote Sens. Appl. Soc. Environ.* **2026**, *42*, 102113.

Disclaimer/Publisher's Note: The statements, opinions and data contained in all publications are solely those of the individual author(s) and contributor(s) and not of MDPI and/or the editor(s). MDPI and/or the editor(s) disclaim responsibility for any injury to people or property resulting from any ideas, methods, instructions or products referred to in the content.